



Flux cutting in high- T_c superconductors

V. Vlasko-Vlasov, A. Koshelev, A. Glatz, C. Phillips, U. Welp, and W. Kwok

Materials Science Division, Argonne National Laboratory, Argonne, Illinois 60439, USA

(Received 18 December 2014; revised manuscript received 12 January 2015; published 30 January 2015)

We performed a magneto-optical study of flux distributions in yttrium barium copper oxide (YBCO) crystal under various applied crossed field orientations to elucidate the complex nature of magnetic flux cutting in superconductors. Our work reveals unusual vortex patterns induced by the interplay between flux cutting and vortex pinning. We observe strong flux penetration anisotropy of the normal flux B_{\perp} in the presence of an in-plane field \mathbf{H}_{\parallel} and associate the modified flux dynamics with the staircase structure of tilted vortices in YBCO and the flux-cutting process. We demonstrate that flux cutting can effectively delay vortex entry in the direction transverse to \mathbf{H}_{\parallel} . Finally, we elucidate details of the vortex cutting and reconnection process using time-dependent Ginzburg-Landau simulations.

DOI: [10.1103/PhysRevB.91.014516](https://doi.org/10.1103/PhysRevB.91.014516)

PACS number(s): 74.25.Uv, 74.25.Dw, 74.25.Ha, 75.60.Ch

I. INTRODUCTION

The general magnetic response of type II superconductors is commonly described in terms of the critical state model, where vortices, each carrying a single magnetic flux quantum (Φ_0), enter the sample above the first penetration field H_p , and form a magnetic-flux density gradient, controlled by the average pinning force F_p due to defects trapping the vortices [1]. The flux entry field H_p is related to surface or edge barriers [2–5] and depends on the material properties and on the field/sample geometry. It is defined by the sample shape (effective demagnetization factor) and size, field orientation, the London penetration depth λ and coherence length ξ and can be much smaller or considerably larger than the first critical field H_{c1} of the superconductor.

The flux gradient in the regions where vortices penetrate is determined by the maximum circulating dissipationless screening current J_c . This critical current flows perpendicular with respect to the vortex lines and induces a Lorentz force on the vortices that is equal and opposite to the pinning force F_p . The vortex system appears to be stationary due to this balance of forces and can remain in this state for many decades [6] until thermal creep depins the vortices, thus decreasing J_c and reducing the vortex density gradient.

In the regions where vortices do not enter, smaller Meissner currents screen the external field. Upon increasing field, vortices fill the entire superconductor with maximum density at the boundaries and minimum in the center of the sample, and the critical current flows all over the sample volume, forming loops enclosed in the sample boundaries. With decreasing field, vortices exit the sample forming a negative flux gradient, and the critical currents invert polarity starting from the edge of the sample and extending to the center as the field drops to zero. This intuitive and very physical Bean's critical state scenario, sometimes modified to account for the field dependence of J_c , has been used extensively to quantitatively explain the magnetization loops in superconducting (SC) samples.

However, such a model fails to describe the magnetization of superconductors under crossing and rotating fields [7–10]. In this situation, new vortices entering the sample induce currents that are parallel or inclined to prior introduced vortices, which result in force-free ($\mathbf{J}_c \times \Phi_0 = 0$) or flux-cutting configurations. For example, if an in-plane field is

applied to a SC plate that is initially magnetized with a normal field and hence carries an in-plane J_c , new vortices will be perpendicular to the initial normal flux and parallel (in some parts of the sample) to the in-plane J_c current. Currents flowing parallel the in-plane vortices do not impose any force on them and could reach the depairing current value before any dissipation occurs. In fact, experiments on current-carrying SC wires in the presence of a longitudinal field showed an enhancement of the critical current [11]. However, the dissipation still occurred well below the depairing current density. This was associated with the appearance of helical vortex instabilities that emerge when the self-field of the transport current in the SC wire generates vortex helices on the surface, which are then pushed to the center of the wire by the current-induced Lorentz force [11].

To explain why the above process does not pump longitudinal vortices into the wire, Clem proposed a flux-cutting scenario [12], whereby vortices in the center of the wire with opposing helicity expand towards the surface. The counterrotation and crossing of helices with different pitch and chirality induce cutting and reconnection of vortices into new helices. This negates flux pumping and instead introduces measurable voltage oscillations along the wire [11]. Although estimates of the currents resulting in the helical instability in [12] were too small, the flux-cutting scenario was widely accepted, further developed, and is still considered in various modern models of the critical state [13–17].

The flux-cutting concept is at the foundation of the general critical state (GCS) picture, first formulated by Clem ([8]; see also earlier papers cited there). The GCS models (GCSMs) recognize two different critical currents—a current transverse to the vortices J_c^T , which is responsible for the maximum gradient of induction (\mathbf{B}), and another current longitudinal to the vortices J_c^L , which controls the maximum gradient of angle between the vortices. When transverse currents exceed J_c^T , vortices begin to move translationally and at longitudinal currents larger than J_c^L , they begin rotating, which then leads to flux cutting and *flux consumption* (decay of the absolute value of \mathbf{B}). During flux cutting, which is an intricate and still not well-understood phenomenon [16], noncollinear flux lines should cross and reconnect into new tilted vortices. The flux consumption arises from macroscopic electrodynamics due to the emerging longitudinal electric

field ($\mathbf{E}||\mathbf{B}$) responsible for the negative time derivative of the induction ($\partial B/\partial t < 0$) [8,17]. Both transverse and longitudinal electric fields generated by the vortex motion and rotation cause losses and are described by nonlinear flux diffusion equations. The latter appears in different forms in various GCSMs [9,10,15] but yield essentially the same qualitative picture of the average flux dynamics. Remarkably, none of these models provide a quantitative explanation of the total set of macroscopic physical effects observed in crossing and rotating fields, including the collapse of the magnetic moment and paramagnetism (see Refs. [16,18]). Moreover, there are no consistent microscopic observations of the vortex behavior in the GCS, although some peculiar flux structures that emerge under crossing fields were imaged and reported [19–22]. Campbell [16, p. 11] admits that “we are a long way from even a qualitative understanding of flux cutting and longitudinal currents.” This raises questions regarding the effect of flux cutting and rotation on the magnetization of superconductors.

In this paper, we present magneto-optical (MO) imaging studies of flux distribution in a thin yttrium barium copper oxide (YBCO) single crystal in various crossing magnetic fields. We observe peculiar flux patterns emerging during remagnetization and estimate the corresponding critical currents. In particular, we find advanced penetration of the normal flux along the applied in-plane magnetic field $H_{||}$ and retardation of flux entry transverse to $H_{||}$ under crossed magnetic field conditions. In addition, by cycling crossing fields (ramping up and down $H_{||}$ or H_{\perp}), we directly observe the flux consumption process predicted by Clem [8]. The staircase structure of tilted vortices in anisotropic superconductors and flux-cutting scenario are used to explain our observations. The majority of GCSMs are one-dimensional (1D) in contrast to the clearly three-dimensional (3D) vortex configurations revealed in our experiment. We use physical concepts of existing GCS theories to analyze our results and discuss the relevant factors that should be included in an adequate treatment. Furthermore, we employ time-dependent Ginzburg-Landau (TDGL) simulations in order to obtain a deeper insight into the vortex dynamics in crossed magnetic fields. The simulations show that transverse flux entry occurs via the motion of vortex semiloops and the expansion of left-handed helical vortices and their crossing and reconnection with initial vortex lines. The result is a distinct vortex rotation boundary revealed in our MO images as a high contrast flux front that forms near the crystal edges and propagates to the center of the sample.

II. EXPERIMENT

The sample used in our magneto-optics imaging experiment is a $1130 \times 340 \times 20 \mu\text{m}^3$ rectangular $\text{YBa}_2\text{Cu}_3\text{O}_{7-\delta}$ single crystal with an onset temperature of $T_c = 92.4$ K and a transition width $\Delta T = 0.3$ K, as determined using superconducting quantum interference device (SQUID) magnetometry in 1 Oe perpendicular field. The crystal is mostly untwined, apart from a few narrow twins located near one corner. The sample was placed on top of a cold finger in an optical cryostat, and spatial maps of the normal induction B_{\perp} on the sample surface were imaged with a polarized light microscope using a MO indicator film technique [23]. Values of B_{\perp} were obtained

from the intensity I of the MO images using $I(B_{\perp})$ calibration. Fields along the c axis, perpendicular to the large face of the crystal (H_{\perp}), were produced using a water-cooled solenoid ($H_{\text{max}} \sim 1.2$ kOe). The in-plane field up to 965 Oe along the ab plane of the crystal was supplied via bulk permanent magnets placed outside the solenoid. We created various crossed-field conditions by rotating the permanent magnets around the solenoid axis. For strictly in-plane field studies, we used air-cooled solenoids with a soft iron yoke, yielding fields up to 2.1 kOe. Variations of the vortex distribution were recorded during magnetization cycles with different field orientations, and the trapped flux patterns were imaged after cooling in different fields. We also studied flux behavior with application of H_{\perp} after field cooling (FC) in $H_{||}$ and vice versa and during perpendicular magnetization in the presence of $H_{||}$.

III. MAGNETIZATION UNDER UNIDIRECTIONAL FIELDS

To highlight peculiarities of flux dynamics arising from crossing field effects, we first characterize the sample magnetization in unidirectional fields and then analyze new features that emerge under various configurations of crossing fields.

A. Magnetization in perpendicular field after zero-FC (ZFC)

Flux patterns in thin SC plates in perpendicular fields have been well studied, and we show them only for comparison with other field geometries. Figure 1 presents a rendition of MO images for perpendicular fields obtained at $T = 50$ K. They illustrate the creation of a typical pillow-shaped pattern [Figs. 1(a) and 1(b)] due to the magnetic flux entry from the sample edges (brighter contrast corresponds to larger normal field B_{\perp}). The shape of the pattern arises from strong field screening by the sharp supercurrent turns at diagonals of the sample corners [see Fig. 1(c)] and is usually observed in high-quality thin rectangular SC plates and films [23]. A deeper flux penetration from the top sample side compared with the lower sample side in Fig. 1(b) indicates a lower edge barrier for the vortex entry at the top side. The asymmetry of the flux entry seen in Fig. 1(b) disappears at higher fields when the contribution from the bulk J_c increases and a symmetric envelopelike critical state flux pattern forms over the entire sample, as shown in [Fig. 1(d)]. When the field is decreased to zero, the symmetry of the envelope-shaped pattern remains the same, although the current direction and flux gradients are inverted [Fig. 1(e)]. Subsequent application of a negative field induces the appearance of so-called Meissner holes [21,24] at the flux front between “positive” and “negative” vortices that propagate inside and remagnetize the sample [see Fig. 1(f)]. The Meissner holes are formed by closed vortex loops, which collapse below some minimum diameter dictated by pinning and leave a flux-free cylinder. They carry enhanced currents, and similar to plasma current filaments in magnetic fields, they are unstable to bending, as discussed in detail in Ref. [24]. This results in the local enhancement of B_{\perp} at the flux front that meanders, as illustrated in Fig. 1(f). Note that the unstable meandering of the Meissner hole line occurs in the large monodomain region of the sample and is not caused by twins, as suggested in Ref. [25].

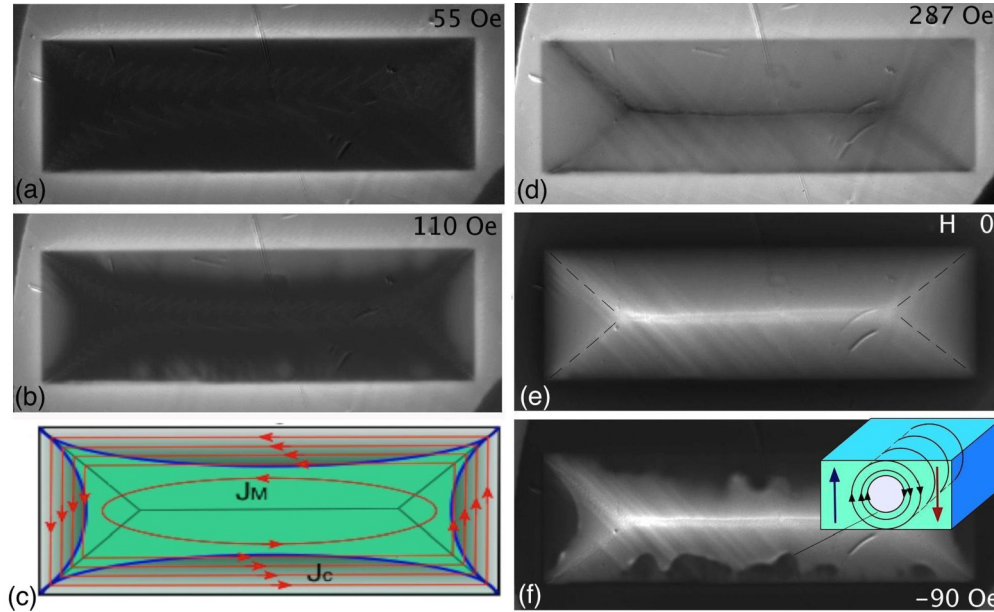


FIG. 1. (Color online) (a) and (b) and (d)–(f) MO images of flux patterns in the magnetic field H_{\perp} applied perpendicular to the ZFC YBCO plate at 50 K. The image intensity corresponds to the field strength and polarity. Bright and dark contrast reveals positive and negative B_{\perp} . Values of the applied field are shown on individual images. (c) A scheme of the pillow shape of the penetrating normal flux supported by critical currents flowing parallel to the sample edges and Meissner currents smoothly circulating in the central flux-free zone. Insert in (f) shows a scheme of the Meissner hole formed at the front between positive and negative normal vortices. Enhanced current along the Meissner hole attracts vortices of opposite polarities as confirmed by the increased bright/dark contrast around the front in (f).

B. FC in perpendicular field

A different picture is observed after FC in $H_{\perp} = 1$ kOe from $T > T_c$ to 50 K and subsequent switching off the field. Here, the trapped B_{\perp} is uniform over the central area of the sample, and the flux exits near the edges. The resulting band of critical state with a gradient of B_{\perp} ($J = J_c$) at the periphery of the sample, formed during the reduction of H_{\perp} to zero, expands towards the center of the sample at higher cooling fields. This band becomes narrower with decreasing final temperature (T_f) when J_c increases. Just after cooling, but before reducing the field, a narrow Meissner rim with slightly decreased B_{\perp} is observed at the sample boundaries. The induction profile in this case is formed by the superposition of current patterns $J(x, T)$ freezing upon reducing T with minimum current $J_c(T \sim T_c)$ in the center and maximum $J_c(T = T_f)$ at the periphery [26].

C. Magnetization in the in-plane fields

1. Magnetic field applied parallel to the long edge of the sample

Since our MO imaging technique is based on the Faraday effect, it traces only perpendicular fields on the sample surface and does not image the spatial distribution of the in-plane component of \mathbf{B} . However, MO patterns at the edges perpendicular to the in-plane field H_{\parallel} can reveal the resulting normal stray fields (H_{\perp}) due to screening or trapping of the in-plane flux, as shown in Fig. 2. The application of H_{\parallel} along the long edges of the ZFC sample causes the field lines to bend near the short sample edges due to partial screening resulting in bright and dark contrast at the short ends [Fig. 2(a)]. With increasing field, the lines of B_{\perp} contrast appear along the twin lamellae on the left revealing vortices tilted towards the c axis at the twin boundaries due to the bending of supercurrents

around the twin planes [Fig. 2(b)] [27]. However, at larger fields, the vortices are forced to align with H_{\parallel} , and the above contrast disappears. After application and switching off the field, the sample is in-plane magnetized, and the contrast at the short ends inverts due to the stray fields of the trapped flux [Fig. 2(c)]. The application and switching off the negative longitudinal field results in another inversion of the contrast [Fig. 2(d)].

An unusual feature revealed in the residual state, which should not occur in isotropic superconductors, is the alternating B_{\perp} contrast, changing from dark to bright along the long top and bottom edges of the sample [Figs. 2(c) and 2(d)]. It is especially distinct at the top edge, which is free of twins. In an isotropic SC plate carrying in-plane flux, both surface and bulk critical currents form closed loops perpendicular to H_{\parallel} . Vortices should bend up and down near the sample edges normal to H_{\parallel} in a narrow strip of the order of the sample thickness. Here, the flux lines diverge from the sample plane similar to magnetic fields exiting a long solenoid. However, vortices should remain parallel to the plate at the sides aligned with H_{\parallel} . In YBCO, the large surface current anisotropy J_s^{ab}/J_s^c can cause a noticeable bending of currents on the side faces of the sample, which will tilt vortices at these faces, as schematically shown in Fig. 3. The stray fields due to the bending of current lines will have components normal to the ab surface near the long edges, resulting in the dark and bright alternating contrast along them, as we see in Figs. 2(c) and 2(d).

It is important to note that there is a *principle* difference in the modes of flux penetration and critical current patterns for an infinite and finite anisotropic SC plate, such as YBCO, in *parallel fields*. In the infinite plate, usually considered in 1D critical state models, vortices enter from the top and

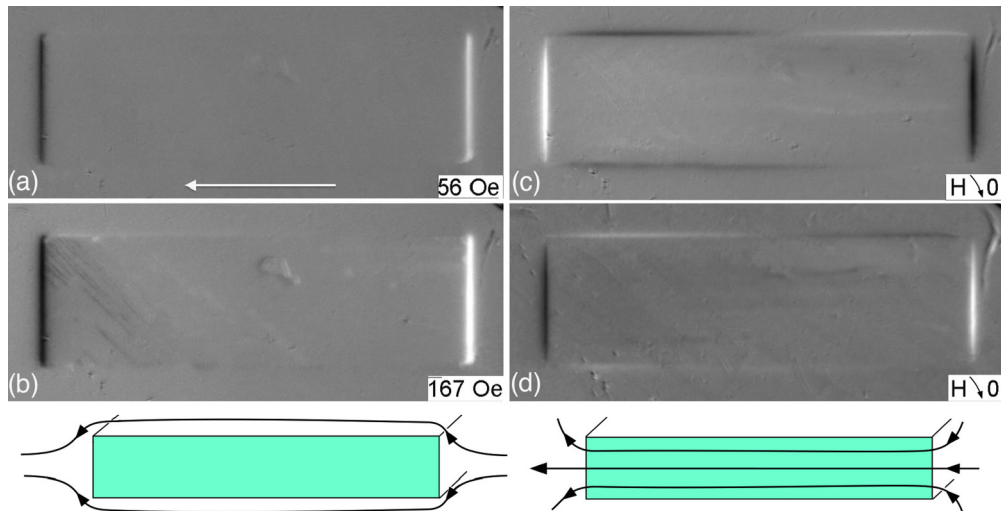


FIG. 2. (Color online) Magnetic patterns in the in-plane field parallel to the long sides of the sample applied after ZFC at 50 K. Schemes of the normal fields revealed by the MO images at application and switching the field off are shown at the bottom. In (b) 45° dark lines stretching from the left top corner appear along the twin lamellae. The pattern in (c) shows trapped flux pattern after application of $H_{\parallel} = 2100$ Oe and switching it off. (d) Shows the same after negative $H_{\parallel} = -2100$ Oe.

bottom surfaces and move perpendicular to the plate plane. The critical currents flow parallel to these surfaces and form induction gradients across the plate thickness $B(z)$ [Fig. 4(a)]. In the finite plate with a reasonable width to thickness ratio, especially in the case of small critical current perpendicular to the surface, the flux penetrates preferentially from the side faces and moves towards the center parallel to the ab surface. For example, in YBCO, J_c^c which hinders sliding of vortices along the cuprate planes, is much smaller than J_c^{ab} that restricts vortex motion across the CuO_2 planes. The critical currents are perpendicular to the ab surface in the main volume of the crystal, and the flux gradient is formed mostly along the plate width [Fig. 4(b)]. This behavior is not accounted for in the 1D infinite plate models. Below, we will discuss some other interesting flux features introduced by the finite size effects.

2. Field parallel to the short sides of the sample

Flux patterns for the in-plane field parallel to the short edges are qualitatively the same as for H_{\parallel} along the long edges. Although here, the strong normal stray fields B_{\perp} of different polarity, revealed by the bright and dark contrast,

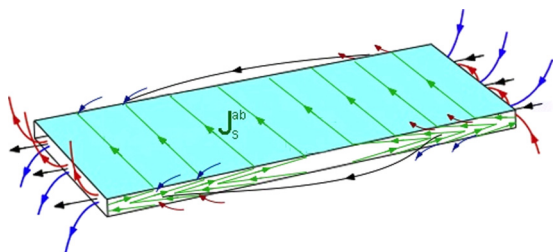


FIG. 3. (Color online) Scheme of the surface currents and edge fields for the trapped flux pattern in Fig. 2(c) accounting for much smaller surface current density perpendicular to the plate ($J_s^c/J_s^{ab} \ll 1$).

appear at opposite long edges (Fig. 5). Probably due to much smaller length of short edges, there is no alternating bright/dark contrast along them, unlike in the case of H parallel to the long edges [Figs. 2(c) and 2(d)].

D. FC in the in-plane field

After FC in in-plane fields $H_{\parallel} > 1$ kOe and switching off H_{\parallel} , the patterns are very similar to those observed in the trapped flux images after magnetization at low temperature. The similarity can be explained by the small in-plane field required for full field penetration $H_{p\parallel}$, which is defined by the small critical current along the c axis. As a result, when $H_{\parallel} > H_{p\parallel}$ is switched off, a critical state with trapped B_{\parallel} is established over the entire sample. The density of trapped in-plane vortices as also the gradient of B_{\parallel} determined by the small J_c^c [see Fig. 4(b)] are comparatively low.

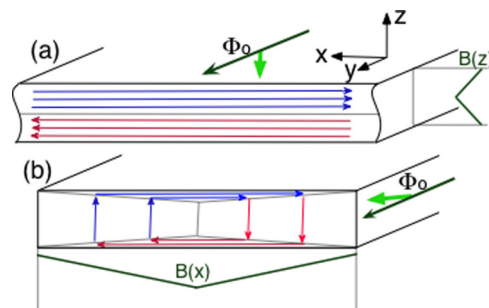


FIG. 4. (Color online) Difference of the critical current patterns for an infinite SC plate (a) and finite slab (b) in the longitudinal in-plane field H_y . Φ_0 arrows show vortices entering from the surface under the Lorentz force along perpendicular short arrows. Major gradients of induction are formed across the thickness, $B(z)$, in (a) and across the width $B(x)$ in (b).

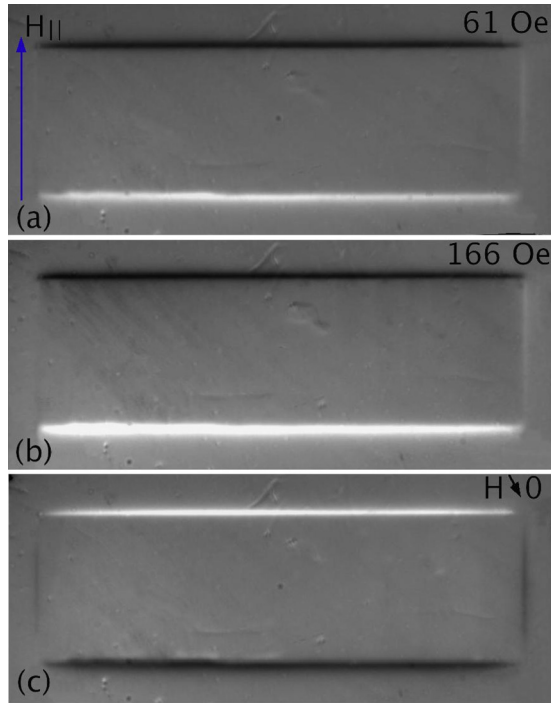


FIG. 5. (Color online) Flux patterns in the in-plane field along short sides. $T = 50$ K. Values of H_{\parallel} are shown in the pictures. In (b), lines at 45° to the long side in the left corner reveal normal fields due to bending of the supercurrents at twin boundaries. Positive and negative perpendicular stray fields at long sides are explained by the same schemes as shown in Fig. 2. The trapped flux pattern in (c) is obtained after application of $H_{\parallel} = 2100$ Oe and switching the field off.

IV. MAGNETIZATION OF THE SAMPLE WITH TRAPPED FLUX BY CROSSING FIELDS

A. H_{\perp} applied to the sample with trapped B_{\parallel}

Application of a perpendicular field H_{\perp} to the sample with a trapped longitudinal in-plane flux results in vortex patterns very similar to the case of normal field magnetization in the absence of trapped B_{\parallel} (Fig. 1). The initial dark and bright contrast due to the trapped in-plane flux at the short edges [see Fig. 2(d)] disappears at relatively small H_{\perp} , and all edges acquire identical bright contrast due to enhanced normal field at the edges. The images are the same when H_{\perp} is applied to the sample with trapped B_{\parallel} obtained after FC in H_{\parallel} or after application and switching off H_{\parallel} at low temperatures. The field penetration depth of the normal induction at fixed values of H_{\perp} is practically the same as in the absence of the in-plane flux. The lack of any noticeable effect of trapped B_{\parallel} on the normal flux penetration is a consequence of the small density of the trapped in-plane vortices, which can be supported by small critical currents along the c axis [see Fig. 4(b)]

B. H_{\parallel} applied along the sample with trapped B_{\perp} : Flux consumption

The situation is quite different when the in-plane field H_{\parallel} is applied to the sample with trapped flux B_{\perp} , normal to the

sample surface. Figure 6 illustrates the entry of the in-plane field aligned with the long edges of the sample following the application and switching off of a perpendicular $H_{\perp} = 1$ kOe at 50 K. Initially, the trapped B_{\perp} is maximum (bright contrast) in the middle of the sample and produces negative stray fields (dark contrast) around the sample perimeter [Fig. 6(a)]. With increasing field H_{\parallel} , the intensity of the central B_{\perp} zone decreases, starting from the short edges in an asymmetric fashion [Fig. 6(b)]. The asymmetry is expected due to the self-fields of the trapped normal flux, which have opposite in-plane components at the opposing short edges. At larger fields, brighter sharp fronts form at the long sides [Fig. 6(c)] and move very slowly towards the center with increasing H_{\parallel} . The sharp contrast of the flux fronts is defined by the enhanced currents along them. This increased current exceeds the critical current J_c^{ab} that supports the trapped B_{\perp} at the center. The slow mobility of the fronts elucidates the retardation of the entering in-plane flux by the normal vortices. As discussed in Sec. IV A, the trapped longitudinal vortices of relatively low density controlled by small J_c^c can easily slide along the ab planes and hardly delay the entry of B_{\perp} . In contrast, the large density of strongly pinned normal vortices defined by the high J_c^{ab} form a noticeable barrier for the entry of in-plane flux. A similar conclusion was obtained from the analysis of the macroscopic magnetization curves of grains of melt processed YBCO in crossing fields [28]. A slow entry of B_{\parallel} from the long sides could be due to the small value of critical currents induced by H_{\parallel} . They flow along the c axis near the long edges ($J_c^c \ll J_c^{ab}$) and do not provide strong enough Lorentz force to move the in-plane vortices across the pinned c axis oriented vortices. However, this explanation seems to be insufficient. The increased current at the horizontal sharp flux fronts in Fig. 6(c) indicates that the main retardation of the in-plane flux occurs at the fronts where the entering in-plane vortices and the trapped c axis vortices have the largest relative misalignment and flux cutting occurs.

With increasing in-plane field, narrow stripes of in-plane flux stretching along the field direction enter from the right short side, while a wider in-plane flux band advances from the left side [Fig. 6(c)]. Upon decreasing H_{\parallel} from a maximum of 2100 Oe, the asymmetry of the flux pattern flips sides showing narrow stripes of the in-plane flux on the left and wider in-plane band on the right. We associate the appearance of the in-plane flux stripes in both increasing and decreasing H_{\parallel} with the inhomogeneous bending of vortices near the sample surface. As shown in Fig. 6(f), with increasing H_{\parallel} , the in-plane flux stripes form at the short edge where the induced screening current J_i (on the top surface) has the same direction as J_c^{ab} supporting the trapped normal flux B_{\perp} . Possibly, current enhancement above J_c^{ab} or tilt of vortices towards their angular instability range (see, e.g. [29] and references there) results in meandering of the supercurrents and inhomogeneity of the vortex bending. Near the opposite short edge, where J_i is antiparallel to J_c^{ab} , a wide band of the in-plane flux appears. At decreasing H_{\parallel} , J_i reverses and narrow longitudinal stripes form on the left short edge, where the tails of the in-plane vortices tilt inhomogeneously up. When $H_{\parallel} = 0$ the normal flux region, B_{\perp} , remains in the center, surrounded by wide B_{\parallel} zones on the left and on the right [Fig. 6(d)]. Also, narrow bands of decreased B_{\perp} form at the long edges. The maximum

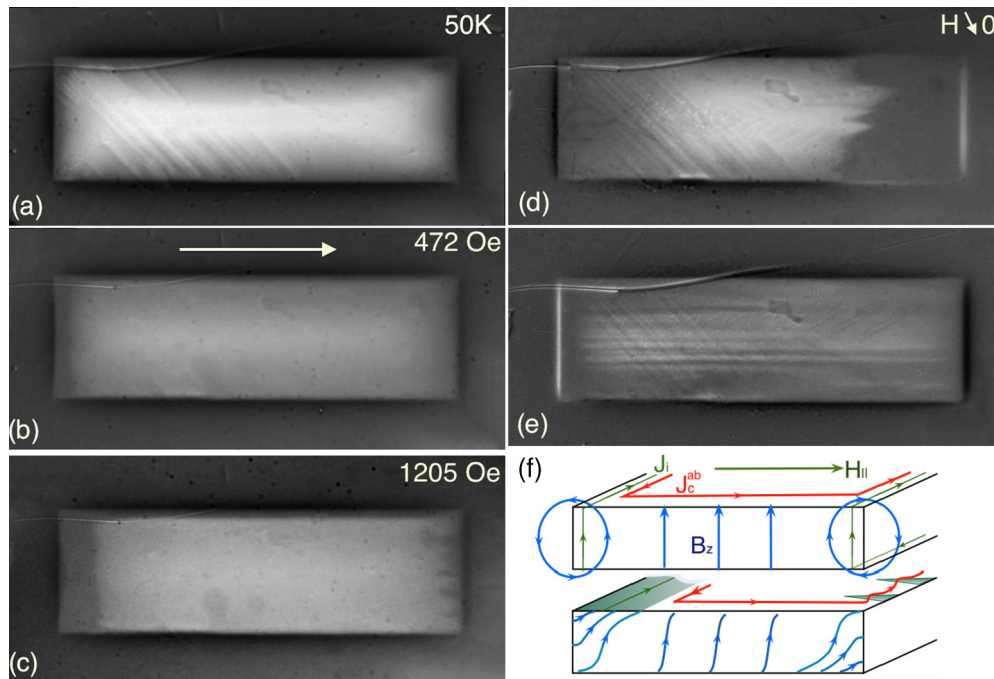


FIG. 6. (Color online) Application of the in-plane field along the long sides to the sample with trapped normal flux shown in (a). The residual flux pattern in (d) remains after application of max $H_{\parallel} = 2100$ Oe, and the domain structure in (e) emerges after following cycling the field to -2100 Oe and back to 0. (f) Shows a scheme of changes in the flux structure and current distribution corresponding to (c).

B_{\perp} in the middle of the sample drops by a factor of ~ 2 [Fig. 6(d)] compared to the initial state of Fig. 6(a). The resulting flux pattern illustrates the effect of suppression of the magnetic moment by crossing fields, which was observed earlier in macroscopic magnetic measurements [10,28,30,31]. Accounting that the in-plane flux density supported mostly by J_c^c is smaller than the density of the initial trapped B_{\perp} supported by J_c^{ab} , the wide incursion of the B_{\parallel} zones near the short ends of the sample in Fig. 6(d) can be considered as direct proof of Clem's prediction of the flux consumption due to remagnetization by crossing fields [8]. With successive cycling of H_{\parallel} to ± 2.1 kOe, the width of the normal flux zone in the center consistently shrinks, and the average B_{\perp} further decreases. At some small value of the remaining B_{\perp} , we observe the appearance of flux stripes carrying vortices with different tilt angles. They remain after switching off H_{\parallel} [Fig. 6(e)] and are similar to vortex domains observed after cooling in tilted fields [32]. The stripes disappear upon subsequent increase of H_{\parallel} .

C. H_{\parallel} applied across the sample with trapped B_{\perp}

Qualitatively similar patterns are observed when the in-plane field oriented parallel to the short edges is applied to the sample with trapped B_{\perp} (Fig. 7). However here, the stripes of in-plane flux enter from the long sides (Figs. 7(b)–7(d)), and sharp fronts with increased currents [Figs. 7(c) and 7(d)] appear near the short sides. The effect of the in-plane field on the suppression of B_{\perp} is noticeably stronger than that of H_{\parallel} applied along the long sides. Already, after first application of 2.1 kOe and switching the field off, the sample becomes in-plane magnetized [Fig. 7(e)]. This clearly shows

the importance of the finite size and shape effects on the vortex dynamics.

V. MAGNETIZATION BY H_{\perp} IN THE PRESENCE OF H_{\parallel}

In the following experiments, the sample was cooled in a constant in-plane field of $H_{\parallel} = 965$ Oe oriented along the long or short sample edges. It was produced by permanent magnets, which were arranged outside the perpendicular field solenoid and remained in place during application of H_{\perp} .

A. H_{\parallel} parallel to the long edges

After cooling in the presence of a large longitudinal field $H_{\parallel} = 965$ Oe, there is no MO contrast to the sample. The absence of the contrast corresponds to a small Meissner flux expulsion, preserving homogeneous density of the in-plane flux coinciding with H_{\parallel} . After application of a small perpendicular field, a typical bright rim of enhanced H_{\perp} forms at the sample edges [Fig. 8(a)]. With increasing field, an anisotropic penetration of B_{\perp} occurs. Faster entry of the normal flux starts at the short edges of the sample through the extension of arch-shaped smooth fronts in the direction of H_{\parallel} . Much slower flux fronts with sharp contrast move across H_{\parallel} from the long edges [Figs. 8(b) and 8(c)]. The easy penetration in the direction of H_{\parallel} and delayed entry of B_{\perp} across H_{\parallel} correspond to a much smaller current density perpendicular to the in-plane field and increased current parallel to the field. A similar anisotropic B_{\perp} distribution was reported in [19,20] for normal magnetization of a YBCO plate in the presence of in-plane field. Our well-defined sample geometry and higher resolution shows more details of the vortex dynamics and

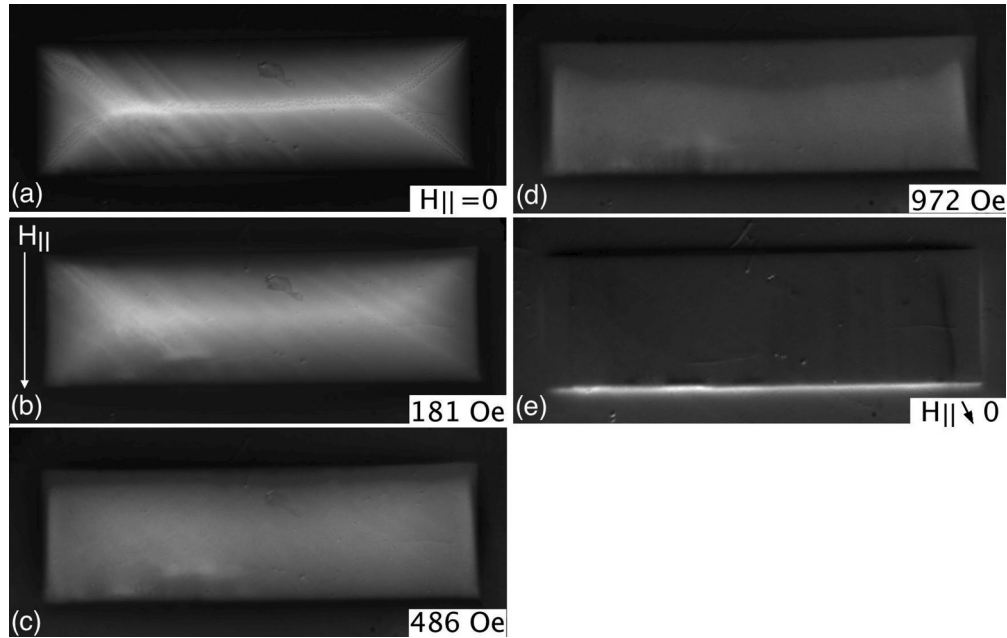


FIG. 7. Application of the in-plane field along short sides in the presence of the trapped normal flux. $T = 50$ K. (e) the normal flux is totally wiped out after increasing H_{\parallel} to 2100 Oe and reducing back to 0.

clearly reveals the enhanced current near the long edges of the sample. Remarkably, there is no asymmetry in the entry of B_{\perp} from the left and right short edges in contrast to Brandt's model for in-plane magnetized stripe under perpendicular fields [[33]; Fig. 9(a)]. It could be that at large enough normal fields, similarly tilted vortices dominate the flux structure at both short edges. However, more likely, the symmetric entry, which we observe even at smallest H_{\perp} , can be due to the staircase structure of bending vortices. Such a structure with normal flux pancakes moving inside the sample along the in-plane Josephson-like strings [Fig. 9(b)] is preferred in layered superconductors under tilted fields with moderate B_{\perp} ([34–36,29]) and can be realized in our case. The attractive coupling between pancakes and Josephson vortices [37] assists “sliding” of the pancake stacks along the in-plane field and lowers the regular pinning potential. Our estimates of the critical currents, discussed below, show about three times smaller J_c for vortices entering along H_{\parallel} compared to case of the purely normal field.

A possible confirmation of the staircase vortex scenario is a considerable reduction of the anisotropy of B_{\perp} penetration at larger H_{\perp} [Fig. 8(d)]. When the normal field reaches ~ 500 Oe ($\sim 1/2$ of H_{\parallel}), the B_{\perp} pattern acquires the envelope-like shape characteristic of the isotropic in-plane currents [Fig. 8(e)]. This can be associated with transition of the staircase vortices into tilted stacks of pancakes with increasing H_{\perp} . Moreover, the symmetric but inverted envelopelike pattern remains after ramping the normal field up-to 900 Oe and then switching it off [Fig. 8(f)]. However, unlike after the application of H_{\perp} in the absence of H_{\parallel} [see Fig. 1(e)], the remnant state in Fig. 8(f) shows a deeper smooth entry of negative B_{\perp} from the short edges and sharp contrast fronts (increased currents), entering into the sample at a much smaller distance from the long edges. The trapped flux pattern in Fig. 8(f) reveals

also some features in the corners of the sample that do not appear in the absence of H_{\parallel} . Here, the lines of sharp current turns (maximum bright contrast, i.e., maximum B_{\perp}) depart from diagonals of the sample corners [see dashed line in Fig. 8(f)], unlike in the pure H_{\perp} case [Fig. 1(e)]. In Fig. 8(f), the bright lines of maximum B_{\perp} start at some distance from the corners and cross at a smaller angle compared to the case of $H_{\parallel} = 0$. The similar shape of the lines of sharp current turns is observed in the full penetration pattern of Fig. 8(d) (dark lines, minimum B_{\perp}). A possible explanation could be an enhanced edge barrier for vortex entry across H_{\parallel} and an increased ratio of critical currents along and across H_{\parallel} ($J_c^{\parallel}/J_c^{\perp} > 1$), as shown in the schematic of Fig. 10(b). The increased J_c^{\parallel} is associated with a delayed entry of tilted vortices with negative B_{\perp} caused by the stray fields of the trapped flux, across trapped tilted vortices with positive B_{\perp} . The new entering vortices are at an angle to the trapped vortices, and their penetration should be accompanied by rotation of the flux lines. It is believed that the flux rotation proceeds through the flux cutting and reconnection process, which occurs at increased longitudinal currents [8–10,14,15,17]. The flux cutting was considered in [20] as a possible reason for the suppressed vortex entry across the longitudinal flux. Here, we show evidence supporting such an explanation.

The application of a *negative* normal field reveals similar preferential penetration of $-B_{\perp}$ along H_{\parallel} [Fig. 8(g)]. Here, sharp fronts of the negative normal flux moving from the long sides carry a concentration of opposite normal fields (bright/dark contrast along the front), revealing strongly enhanced currents along them. With increasing $-H_{\perp}$, the flux distribution approaches the envelopelike structure [Figs. 8(h) and 8(k)], showing that currents in the ab plane become nearly isotropic. A similar but inverted B_{\perp} pattern remains after switching off H_{\perp} [Fig. 8(l)].

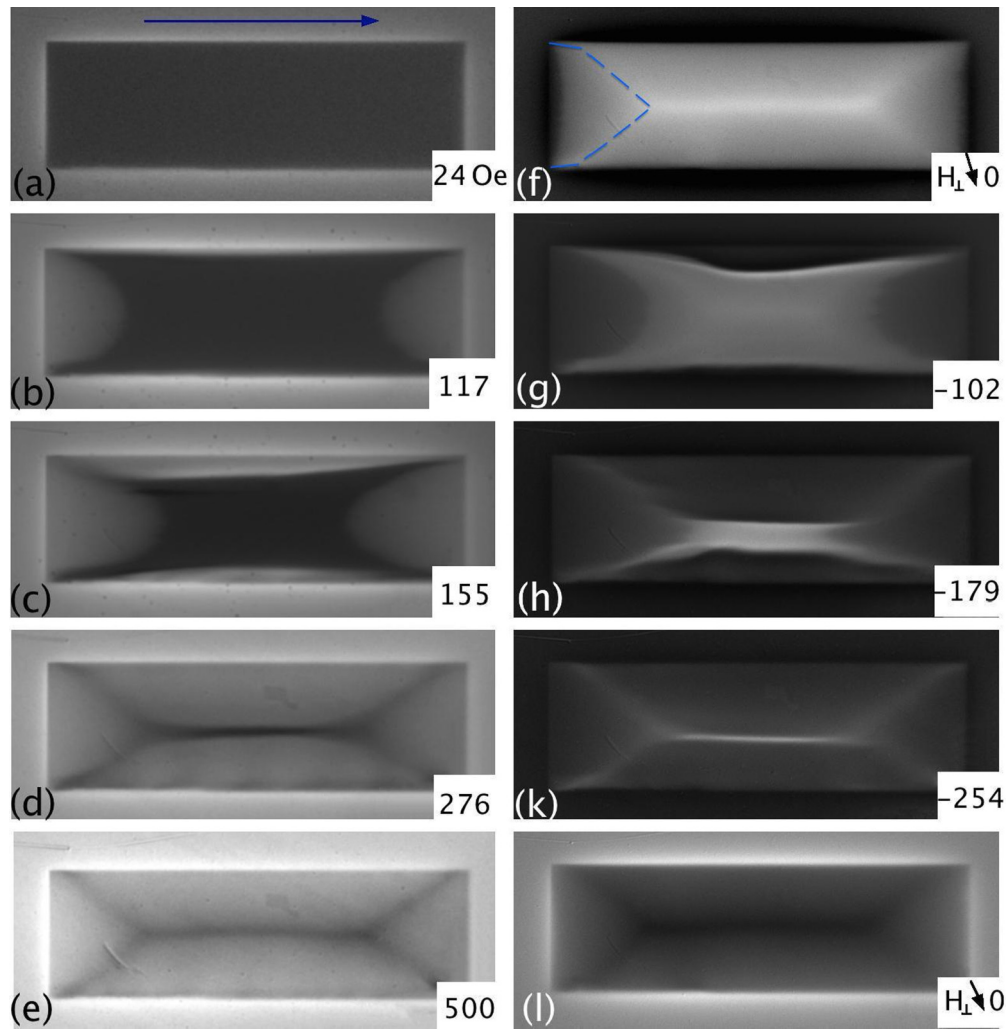


FIG. 8. (Color online) Application of perpendicular field in the presence of $H_{\parallel} = 965$ Oe along the long sides. $T = 50$ K. Maximum value of applied H_{\perp} was ± 900 Oe.

Multiple lines with enhanced B_{\perp} contrast around them were observed in [20], after application of an alternating normal field to a YBCO crystal in the presence of a dc in-plane field. They

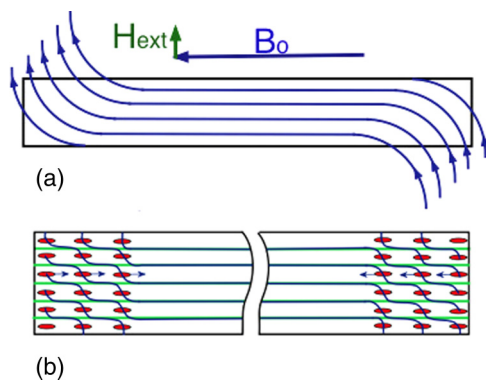


FIG. 9. (Color online) (a) Scheme of the vortex bending due to application of the normal field in the presence of the in-plane field. (b) Staircase vortex structure of bent vortices near the edge. Arrows show the motion of pancake vortices, which symmetrically bring B_{\perp} inside the sample.

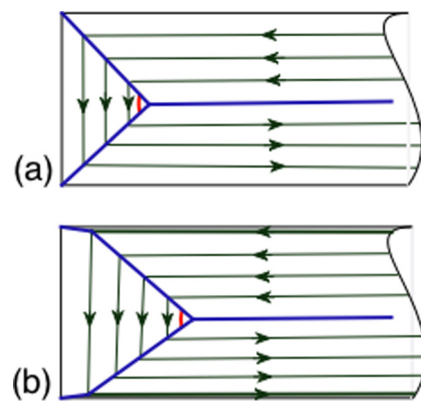


FIG. 10. (Color online) Scheme of lines of sharp current turns in the corners of rectangular plate due to enhanced surface current along horizontal sides and reduced currents in perpendicular direction. (a) Currents at the total penetration of B_z turn at the corner diagonals in the absence of in-plane field H_{\parallel} . (b) In the presence of H_{\parallel} along the long sides, the current turn lines are shifted from the corners and their mutual angle is reduced.

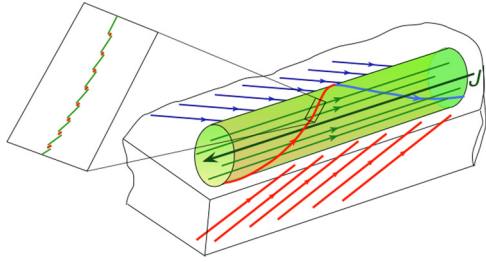


FIG. 11. (Color online) Flux structure at the front between misaligned vortices during remagnetization by the normal field in the presence of the in-plane field. Near the top and bottom parts of the plate, helical vortices have staircase structure. In the case of short pitch, the sides of helices are formed by tilted stacks of pancake vortices. Helices with long pitches should have staircase structure over the whole length. The enhanced current in the front area forms a straight cylinder along the edge of the sample parallel to H_{\parallel} . Small arrows show the polarity of vortices and thick arrow shows the current direction in the cylinder with in-plane vortices.

were associated with bundles of helical vortices carrying large force-free *helical currents*. In a strongly anisotropic material, one could expect a complex vortex structure at the boundary between vortices with opposite B_{\perp} . Vortices *slightly tilted* from the ab plane should be composed of staircase Josephson-like segments with up or down magnetized pancakes. *Strongly tilted* vortices are represented as shifted pancake stacks. At the front between the trapped and entering vortices with opposite normal flux components but with the same \mathbf{B}_{\parallel} , there should be a helical flux configuration wrapped around in-plane vortices in the middle (see schematic in Fig. 11). Top and bottom segments of helices, close to the ab plane, will have staircase structure while their side segments, tilted up or down, will consist of tilted pancake stacks, if their angle from the ab plane is large enough. Note that this angle is not limited by the applied normal field but is caused by the enhanced current along the front resulting in increased B_{\perp} around it. Unlike small vortex loops collapsing inside a Meissner hole due to the line tension, helical vortices with relatively large pitch experience much smaller contraction forces and can be easily stabilized by pinning. Also, their collapse into straight longitudinal vortices will be prevented by the vortex cutting process. Currents along the front will have a substantial component along forming front vortices, depending on the vortex angle with respect to the front axis. They can be much larger than limited by pinning critical currents, which flow perpendicular to vortices and define their transverse motion. The increased currents will cause the enhancement of opposite B_{\perp} components around the front, as we observe in the experiment. The front motion will occur by the asymmetric collapse of helices with increasing negative H_{\perp} . This process involves both flux cutting and vortex depinning and requires larger critical current than that for the regular vortex motion across the pinning potential. If we assume that enclosed helices forming the front occupy a cylinder with a homogeneous longitudinal current density J_{\parallel} , the pitch P turns out to be the same for all helices. $P = 2\pi R H_{\parallel} / H_{\perp}(R)$ at radius R from the cylinder center, where the perpendicular field of the current is $H_{\perp}(R) = m_0 I / 2\pi R$ and the total current within R is $I = \pi R^2 J_{\parallel}$. The resulting pitch $P = 4\pi H_{\parallel} / \mu_0 J_{\parallel}$ becomes

independent of R . This simple estimate should be corrected for an anisotropic material, where the front structure is more complex. Obviously, the current density will decay away from the axis of helices as vortices tilt from the ab plane and from the current direction. Summarizing, instead of the force-free currents following helical trajectories, we expect a strong axial current along the front between $+$ and $-B_{\perp}$ vortices, with current density increasing towards the front center.

B. H_{\parallel} parallel to the short sides

The basic features of the normal flux penetration in the presence of H_{\parallel} along the short edges are qualitatively similar to those observed for H_{\parallel} parallel to the long edges. At small H_{\perp} , the normal c axis flux is first screened by the ab currents, which enhance the perpendicular fields at the sample edges [bright contrast in Fig. 12(a)]. With increasing H_{\perp} , the normal c axis flux start entering from the long crystal edges forming multiple narrow stripes along H_{\parallel} [Fig. 12(b)]. The entry of B_{\perp} is somewhat asymmetric due to the different edge barriers at opposite long edges [compare with Fig. 1(b)]. With increasing field, the stripes form jagged fronts and penetration of B_{\perp} from the long sides become more symmetric [Fig. 12(c)]. Once the top and bottom flux fronts reach the center of the crystal, sharp fronts aligned with H_{\parallel} begin to penetrate from the left and right short edges [Fig. 12(d)]. These fronts have bright/dark contrast, revealing increased currents along them. The external field concentration along the short edges, caused by the screening currents along them, is higher (the edge contrast is brighter) than that along the long edges [Fig. 12(d)]. This confirms that currents parallel to \mathbf{H}_{\parallel} are stronger than J_c across \mathbf{H}_{\parallel} . A further increase of H_{\perp} causes the stripe flux pattern to fade and the sharp fronts from the short sides to penetrate deeper into the sample [Fig. 12(e)]. At even larger H_{\perp} , the jagged flux fronts soften and the flux pattern evolves into an envelope-like shape [Fig. 12(f)], similar to that shown in Fig. 1(c) for the normal field [Fig. 1(c)].

After decreasing H_{\perp} from a maximum applied field of 850 Oe, the envelope-like pattern flips its contrast (dark symmetric lines become bright) but keeps the same symmetry [Fig. 12(g)] similar to the case of purely normal c axis field [Fig. 1(e)]. However, when H_{\perp} is reduced to zero, narrow bands of negative normal flux with stripes along \mathbf{H}_{\parallel} enter from the long edges to a noticeable distance. As in the presence of H_{\parallel} along the long sides, the negative flux entry is strongly anisotropic. It is preferential along H_{\parallel} and delayed across H_{\parallel} , causing a sharp contrast near the short edges, as shown in Fig. 12(h). Application of a negative H_{\perp} advances the negative B_{\perp} penetration from the long edges [Fig. 12(k)]. Concurrently, flux fronts with sharp, dark/bright contrast, i.e., carrying increased current, slowly move from the short edges [Fig. 12(l)]. At larger negative field, H_{\perp} the normal c axis flux distribution transforms into the envelopelike pattern, as discussed above.

VI. COMPARISON OF NORMAL FLUX PATTERNS WITH AND WITHOUT IN-PLANE FIELD

In Fig. 13, we compare flux patterns for the same normal field $H_{\perp} = 155$ Oe, applied at 50 K, following zero FC and

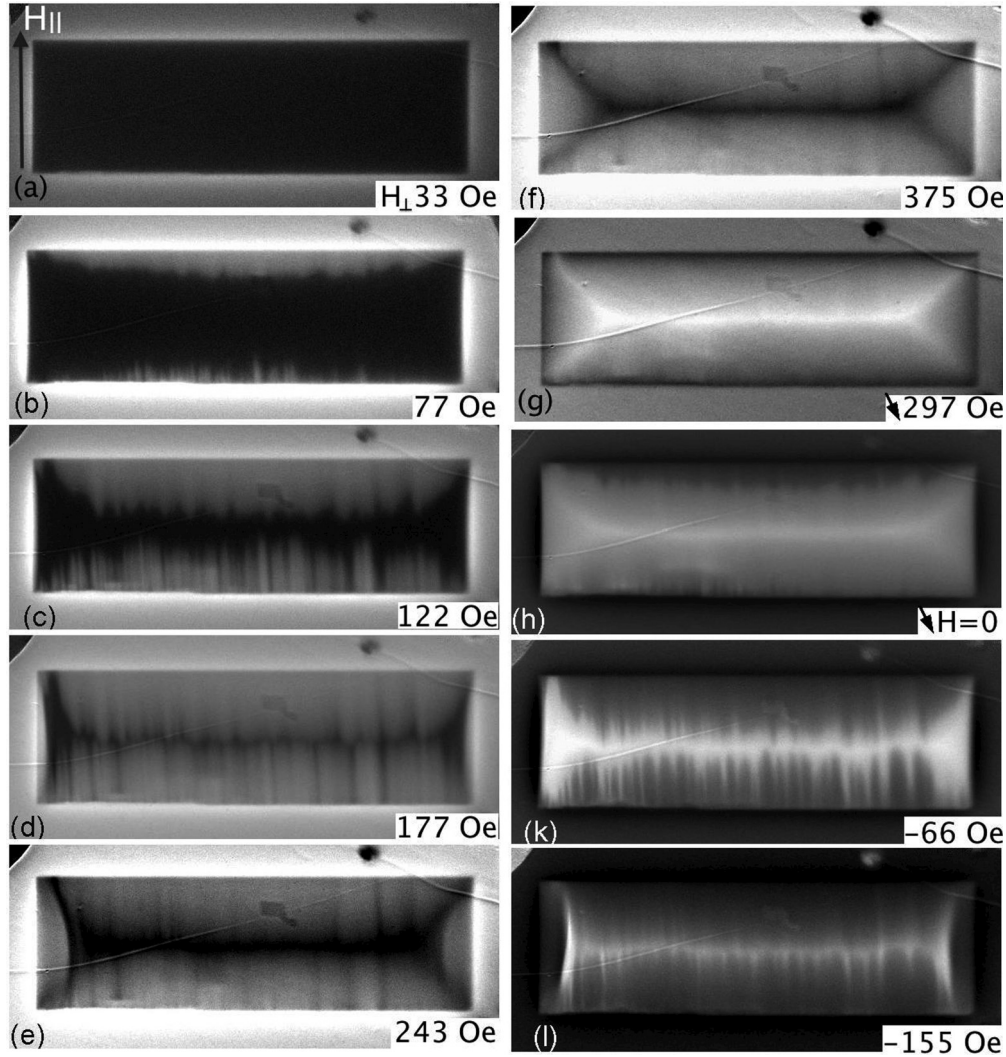


FIG. 12. Application of perpendicular field, H_{\perp} , in the presence of the in-plane field, $H_{\parallel} = 965$ Oe, across the sample length. The sample was cooled in H_{\parallel} to 50 K. (a)–(f) increasing H_{\perp} , (g) and (h) decreasing H_{\perp} from max of 900 Oe, (k)–(l) increasing negative H_{\perp} . Field values are shown on the pictures.

following cooling in longitudinal and transverse in-plane fields of $H_{\parallel} = 965$ Oe. Compared with the ZFC sample [Fig. 13(a)], the normal c axis flux penetration for H_{\parallel} applied along the long edge [Fig. 13(b)] is twice as deep along the applied in-plane field direction, and flux penetration from the long edge is nearly twice as small. Similarly, in the transverse in-plane field [Fig. 13(c)], we also observe easy flux entry parallel to the applied in-plane field direction. However, the initial B_{\perp} entry at the short edges is suppressed much stronger in this case. The difference is associated with the finite size and the shape of the sample, which result in different current flow patterns and cause different flux entry behavior, depending on the direction of H_{\parallel} .

The induction profiles $B_{\perp}(x)$ and $B_{\perp}(y)$, across the short and long edges of the sample, respectively, are shown in Fig. 13(d). To obtain changes in the critical currents we made numerical fits to these profiles using a model current distribution. We assumed a constant critical current J_c^{fit} for the penetrating B_{\perp} and a constant edge current J_E within a thin layer along the sample boundaries. In the flux-free

center zone, the current was approximated by the 1D Meissner solution for a long SC strip [38,39], with varying maximum current J_M . A more accurate approach would use an elliptic 3D shape to model the flux front [40]. However, with our thin sample geometry, we assumed a simplified two-dimensional (2D) current distribution that is homogeneous throughout the thickness (see Fig. 14) and calculated B_{\perp} at $2 \mu\text{m}$ height above the surface. The values of J_c , J_E , and J_M were adjusted to fit the experimental B_{\perp} profiles. The obtained values of the critical current for the entry of B_{\perp} along H_{\parallel} [$J_c^{\text{al}} \sim 4 * 10^4 \text{ A/cm}^2$ for $B_{\perp}(y)$ in Fig. 13(c)] turned out to be about three times smaller than in the absence of H_{\parallel} [$J_c^{\text{ZFC}} \sim 1.4 * 10^5 \text{ A/cm}^2$ for $B_{\perp}(y)$ in Fig. 13(a)]. Fitting different B_{\perp} steps at opposite long sides required different edge currents J_E . However, it did not introduce large changes to the value of the fitting critical currents. Estimates of J_c from the penetration of the applied H_{\perp} using formulas for a thin infinite strip of width $w = 2a$ [38,39] $J_c = \pi H_{\perp} / (h * \text{ArcCosh}(a/b))$, where b is the distance from the strip middle line to the flux front and h is the strip thickness, yielded similar values $J_c^{\text{al}} \sim 4.3 * 10^4 \text{ A/cm}^2$

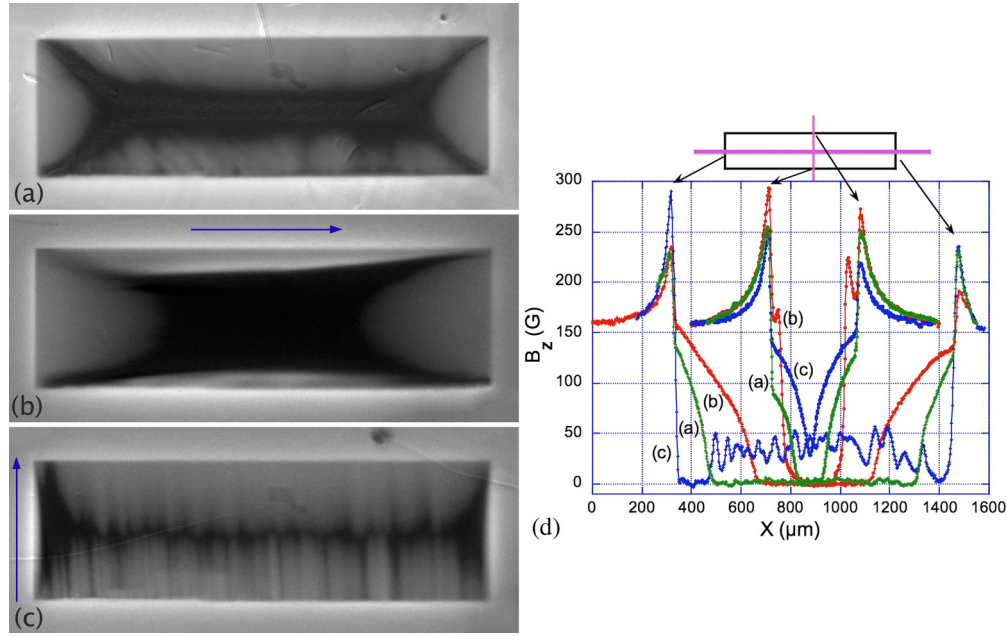


FIG. 13. (Color online) Comparison of flux patterns in the same perpendicular field $H_{\perp} = 155$ Oe applied in the absence (a) and in the presence of the in-plane field $H_{\parallel} = 965$ Oe parallel (b) and perpendicular (c) to the long sample sides. $T = 50$ K. Appropriate B_{\perp} profiles along and across the sample are shown in (d).

and $J_c^{ZFC} \sim 1.3 \times 10^5$ A/cm². The close values of J_c obtained by different approaches confirm the validity of our 2D model. $B_{\perp}(y)$ for the perpendicular flux entry across H_{\parallel} [Fig. 13(b)] was approximated by $J_c \sim J_c^{ZFC}$ but with a Meissner-like current of increased density $J_M^{\max} \sim 10 J_c^{ZFC}$ at the front of B_{\perp} . The exact solution for partial flux penetration in a thin SC strip predicts $J_M^{\max} = J_c^{ZFC}$ [38,39]. It is expected that in a thin YBCO plate the current at the normal flux front can slightly increase due to the bending of vortices and enhanced pinning on the CuO planes [40]. In our case, the large fitting value of J_M^{\max} is much higher than predicted in [40]. It corresponds to the observed strong current line at the boundary, where the in-plane vortices meet the normal flux. The main delay for the normal flux entry occurs at this crossing vortex front.

As described in Secs. V A and V B, at higher normal c axis fields ($H_{\perp} \sim 1/2 H_{\parallel}$) the strong anisotropy of B_{\perp} penetration disappears, resulting in the symmetric envelope-like flux patterns [Figs. 8(d)–8(f) and Figs. 12(f) and 12(g)]. This can be associated with changes in the flux motion mode due to transformations of the vortex structure. At large H_{\perp} , Josephson-like segments disappear, and vortices become curved pancake stacks upon tilting from the ab plane. It was

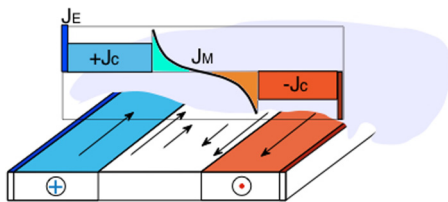


FIG. 14. (Color online) Scheme of the current distribution used for fitting B_{\perp} profiles in Fig. 12(d).

proposed in [33] that the delayed B_{\perp} entry transverse to H_{\parallel} can be associated with the in-plane orientation of screening H_{\perp} currents, which are closely aligned with vortices and impose only a small Lorentz force. Therefore, advancing the flux front will require increased longitudinal current densities near the edges parallel to H_{\parallel} . Another reason for the retarded normal flux entry due to the in-plane vortices can be flux cutting. In combination with regular pinning, the flux cutting should further increase J_c .

An unexpected effect is the observed reduction of J_c^{al} , corresponding to the advanced penetration of *tilted* vortices along H_{\parallel} , as compared to J_c^{ZFC} in the purely normal field. Such decreased pinning and the absence of asymmetry in the normal flux entry along H_{\parallel} [Fig. 13(b)] cannot be explained simply by the tilt of vortices from the sample plane due to the screening normal field currents, as suggested in [33]. According to [33], when the normal field is applied to the longitudinally magnetized SC strip, longitudinal vortices should asymmetrically tilt their tails near short ends where the in-plane currents induced by H_{\perp} are transverse to vortices [see Fig. 9(a)]. The reduction of J_c in this case is not expected. We assume that the easy and symmetric motion of B_{\perp} along H_{\parallel} in YBCO is a consequence of the staircase structure of vortices at moderate tilt angles from the ab -plane. It can be depicted by sliding of pancake vortices along Josephson-like in-plane flux strings, as discussed in Sec. V A [Fig. 9(b)].

VII. BRIEF REVIEW OF GENERAL CRITICAL STATE MODELS

Clem was probably the first who clearly formulated the ideas of the GCSMs through a set of electrodynamics equations, yielding a simple solution for the magnetic flux diffusion in superconductors with arbitrary directions of the

flux and current. The basic Bean model, accounting for the motion of vortices by the Lorentz force induced by transverse currents was appended with longitudinal currents causing the mutual twist of vortices. Although the model was purely phenomenological, Clem specified that flux cutting is the mechanism for twisting vortices. A thorough historical review of research preceding Clem's model can be found, e.g., in [8,11,41]. The main result of the model, further developed by Clem and Perez-Rodriguez and then by other researchers (see references in [17]), is the description of induction diffusion when the current components parallel and perpendicular to \mathbf{B} exceed the critical values \mathbf{J}_{\parallel}^c or \mathbf{J}_{\perp}^c respectively. The flux diffusion, and thus dissipation, includes both the transverse vortex motion (at $\mathbf{J}_{\perp} > \mathbf{J}_{\perp}^c$) and rotation (at $\mathbf{J}_{\parallel} > \mathbf{J}_{\parallel}^c$). The latter occurs through the vortex cutting mechanism and results in a negative dB/dt corresponding to *flux consumption*. In [8], \mathbf{J}_{\perp}^c and \mathbf{J}_{\parallel}^c are independent and form rectangular parametric current space ($J_{\perp} < |\mathbf{J}_{\perp}^c|$, $J_{\parallel} < |\mathbf{J}_{\parallel}^c|$) of the vortex immobility. However in more recent models, which account for the intimate coupling between vortex motion and rotation, \mathbf{J}_{\perp}^c and \mathbf{J}_{\parallel}^c are bound by elliptic relations (lossless currents are confined within an ellipse with principle axes \mathbf{J}_{\perp}^c and \mathbf{J}_{\parallel}^c [14,17]). In crossing or rotating fields, there can be a few spatial zones in the sample, where vortices are stable, move under transverse currents, experience cutting (and thus rotation), or both move and cut [13]. This scenario appears in all current GCSMs with some variation in details (see Refs. in [16–18,42]).

Despite multiple papers on the subject, the vortex cutting process still remains elusive. Fisher *et al.* [10,43,44] attempted to introduce it through a phenomenological coefficient $p \ll 1$, representing the probability of flux cutting in kinetic equations for the density and angle of vortices moving under crossing fields. The flux cutting is pictured using two noncollinear sets of vortices, which are mutually oscillating (reminiscent of oscillating vortex planes in the early Clem's model [12]) and advance with an average velocity in the same direction. The resulting electrodynamics equations for induction B and the flux angle θ are qualitatively similar to those in Clem's GCSM, however instead of J_{\parallel} , some combination of J_{\perp}^c , p , and θ defines the angle gradient. Numerical simulations using Fisher's model showed an improved approximation for experimental data obtained in low crossing fields [44].

The latest attempt to describe the flux diffusion in crossing fields was implemented using a functional (F), combining energy changes and dissipation in the moving vortex system [15]. The conditional minimum of F was searched within limitations for possible currents in the superconductor. Basically, these limitations introduce critical currents common to all other approaches. The numerical solutions of the model reproduce a zone for flux consumption (with decreasing absolute value of B), which propagates inside the SC plate upon rotation of the external field, and confirm other qualitative features of different GCSMs. For a detailed overview of this model and various simulation results, see [45].

Unfortunately, most GCS approaches consider only the thin plate geometry in parallel fields allowing for a 1D treatment of the problem, which is different from our experimental situation. Probably, the major exception is simulations of rectangular plates by Brandt and Mikitik [46–50]. However,

these simulations neglect flux-cutting effects, while in our observations they appear to be crucial. Also, the enhancement of the critical current by the in-plane field was explained in these simulations by an effective increase of the length of vortices tilted from the plate normal ($J_c = J_c^0/\cos\alpha$, α -tilt angle) [48,51], whereas we detect strongly enhanced currents only at flux fronts between crossing vortices. The formation and motion of the fronts can be hardly understood without accounting for the flux-cutting process. Another effect, the advanced propagation of B_{\perp} along the applied in-plane field direction, could be explained by Brandt's predictions of enhanced flux relaxation along a narrow strip in crossing longitudinal and normal fields [48]. However, the observed *decreased pinning* for B_{\perp} entering along H_{\parallel} and reduced relaxation transverse to H_{\parallel} are not expected in this model.

So far, we can probably address only the basic concept of flux consumption due to flux cutting as relevant to our observations. It gives a qualitative explanation of the trapped B_{\perp} suppression by sweeping in-plane field [Figs. 6(d) and 6(e)]. We believe that the staircase vortex structure specific for layered superconductors in oblique fields and the flux-cutting process should be accounted to explain the advanced penetration of B_{\perp} along the in-plane field and the delayed entry across H_{\parallel} in YBCO. This claim is supported by the change of B_{\perp} patterns acquiring symmetric envelopelike shape at larger normal fields, when the vortex structure transforms from the staircase into the tilted pancake configuration, resulting in the removal of the vortex motion anisotropy.

VIII. FLUX CUTTING

The idea of flux cutting was first introduced [11,52] to explain unexpected voltage oscillations in current carrying SC wires in the axial magnetic field. Since then, the force free configurations and transverse vortex motion in longitudinal currents were addressed in many theoretical papers but still remain a hypothetical concept. Two crossing vortices should experience a long-range repulsion due to the λ shell of supercurrents, while the intersection of the normal cores will provide their short-range attraction [53]. This could yield *pinning of vortices by transverse vortices*. The resulting pinning potential was first assumed to be very high (about normal core condensation energy), but subsequent calculations showed only moderate values of the cutting barrier U_x [53]. Account of the mutual bending of vortices near the intersection point revealed additional attraction and further reduction of U_x [54–57]. However, the anisotropy ($\Gamma = \lambda_c/\lambda_{ab}$), such as in layered cuprates, was shown to enhance U_x [55]. Furthermore, for lower GL parameters ($\kappa = \lambda_{ab}/\xi_{ab} \sim 10$) and in moderate fields, U_x was found to decrease as $1/\Gamma$ [58]. Later, both London and TDGL simulations by Bou-Diab *et al.*, [59], for typical high- T_c superconductors $\kappa \sim 100$, showed that cutting of two individual vortices can be a complex multistage process involving intricate mutual twisting and recurrent counter-motion of the vortex segments. To clarify how vortex cutting is involved in the penetration of the normal flux in the presence of in-plane vortices, we performed simulations in a weak field regime using the TDGL approach, as described below.

IX. TDGL SIMULATIONS OF THE CROSSING FIELD ENTRY

We solved the TDGL equations numerically in the large λ limit using graphics card processing units (GPUs). Details of the actual implementation can be found in Ref. [60]. In dimensionless units, the equation for the complex order parameter ψ is given by

$$\partial_t \psi + i\mu\psi = \psi - |\psi|^2\psi + [g(\nabla - i\mathbf{A})]^2\psi + \zeta(\mathbf{r}, t)$$

Here, μ is the scalar potential calculated self-consistently using the Poisson equation, \mathbf{A} is the vector potential, and ζ is a thermal noise term. The latter is defined by a correlator $\langle \zeta(\mathbf{r}, t)\zeta(\mathbf{r}', t') \rangle \propto T\delta(\mathbf{r} - \mathbf{r}')\delta(t - t')$. The anisotropy of the YBCO crystal is described by the tensor g , which basically rescales the gauge-invariant gradient in z direction by a factor g . Here, we assumed $g = 5$.

For the vector potential, we used the Landau gauge $\mathbf{A} = y[-B_z, 0, B_x]^T$; z is along the c axis. The unit of length is the zero-temperature coherence length $\xi_0 = \xi_{ab}$, the unit of time is the GL time $\tau_{GL} = \pi/8|T - T_C|$, and the magnetic field is scaled to $B_{c2}(T = 0) = \Phi_0/2\pi\xi_0^2$. The equation is discretized on a regular spatial mesh of $256 \times 256 \times 128$ grid points with physical dimensions of $128 \times 128 \times 64\xi_0^3$. The choice of this moderate volume allowed us to limit the calculation time, while at the same time to realistically capture the dynamics of many interacting vortices. The boundary conditions were periodic in x and z directions and open in y direction (describing a surface of the sample). The minimum time step of the simulation corresponded to $0.1\tau_{GL}$ and $T = T_C/2$.

The system was initialized with a random state (arbitrary amplitudes and phases of the order parameter) and then relaxed in an in-plane magnetic field in the x direction ($B_x = 0.04$) for 80 000 time steps with relatively large noise for quick annealing. This created a dilute vortex lattice, such that individual vortices could be identified. Then a small z component was switched on and slowly increased to $B_z = 0.004$ over the following 220 000 time steps. This simulation took about 6 h on a Fermi-class GPU. Note, that due to the large λ limit the interaction between vortices is not screened exponentially but decays as $\sim 1/r$. However, to study the process of flux cutting this is not a relevant limitation.

Snapshots of the vortex transformations during the application of B_z are presented in a set of pictures discussed below. In these pictures, vortices are visualized by isosurfaces of the order parameter amplitude at value 0.1, shown as green cylinders. As illustrated in Fig. 15, vortices go from mostly in-plane orientation [Fig. 15(a)] through a complicated intermediate state with helical vortices and vortex tilt fronts [Fig. 15(b)], to the out-of-plane alignment [Fig. 15(c)]. Analysis on a smaller time scale reveals multiple crossing and reconnection events between initial vortices, vortex semiloops entering from the sample edges, and helical vortices, which form from straight vortices and expand due to the longitudinal currents induced by changing B_z . Figure 16 illustrates a couple of successive vortex collisions within $150\tau_{GL}$ time interval.

Only at the highest time resolution $0.1\tau_{GL}$ could we follow the details of the crossing process between two individual vortices, as illustrated in Fig. 17. Initially, one of the vortices had the original orientation in the x direction, while the end of

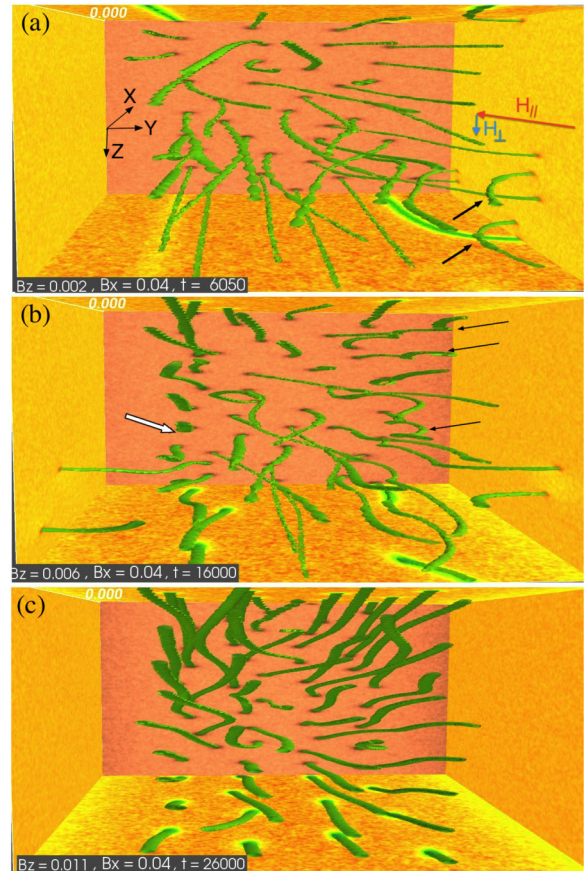


FIG. 15. (Color online) Snapshots of simulated vortex configurations upon application of the vertical field B_z to the sample relaxed in the in-plane field $B_x = 0.04$. Fields are in units of B_{c2} and time in units of τ_{GL} . (a) Initial state at the very beginning of ramping up B_z ($B_z = 0.002$, $t = 6050$). Vortices are mostly aligned with B_x . Arrows near the right surface point to curved entering vortices. (b) Intermediate vortex structure ($B_z = 0.006$, $t = 16000$). There are helical vortices (see thin arrows on the right), expanding due to longitudinal currents J_x induced by B_z . Also, a sharp front of the vortex tilt is formed on the left (thick arrow) (c). Final state ($B_z = 0.011$, $t = 26000$). Vortices tend to align with $\mathbf{B}_x + \mathbf{B}_z$.

another one was pulled along the y surface when B_z was switched on. The tilted vortex moved towards the in-plane vortex due to the Lorentz force of the screening current induced by B_z . Since vortices can only intersect and reconnect when their polarity is opposite, they start mutually bending at a short distance. One of them (V2) forms a local helical step [Fig. 17(a)] before the intersection occurs. When vortices approach, their mutual velocity is substantially decreased. However in the close proximity, when bent segments of vortices become locally antiparallel [see opposite arrows near the point of intersection in Fig. 17(a)], attractive forces come into play and pull the vortices together, accelerating them. After crossing, one of the reconnected vortices forms a tight loop [Fig. 17(b)], which is quickly straightened as the vortices depart from each other. Unlike the double state process for two perpendicular vortices described in [59], the cutting and reconnection occurs as a single event. This is due to asymmetric mutual bending of vortices adopted before crossing and the composition of the

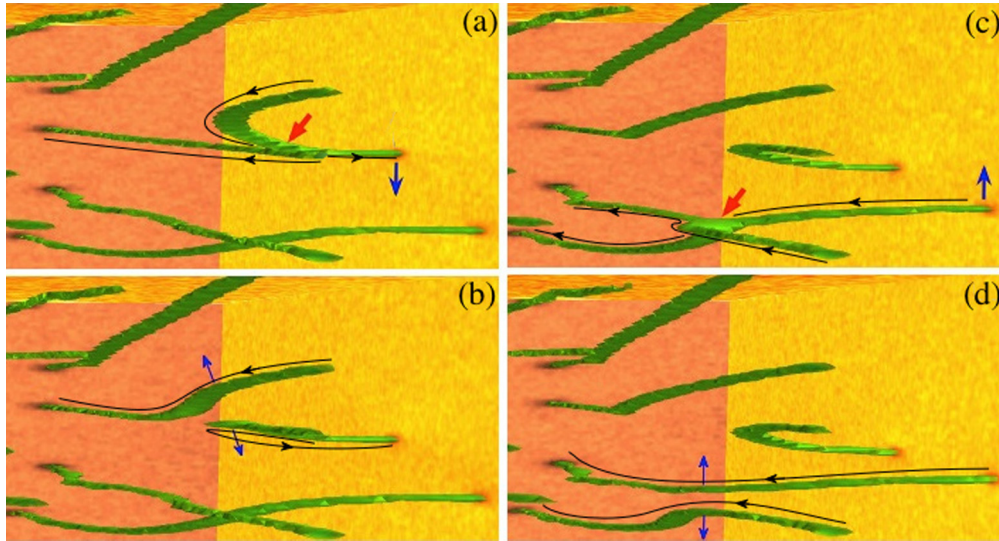


FIG. 16. (Color online) Two successive vortex crossing events near the right side of the sample within $150\tau_{GL}$ time interval. $B_x = 0.04$. (a) $B_z = 0.003$, $t = 10\,000$, (b) $B_z = 0.004$, $t = 10\,050$, (c) $B_z = 0.004$, $t = 10\,100$, and (d) $B_z = 0.004$, $t = 10\,150$. Thicker arrows point to vortex intersections. In (c), the vortex cores are expanded and overlap at the crossing point. Thinner arrows show the direction of the vortex motion. Long thin lines with arrows along vortices show their polarity.

resulting vortices, which consist of the combined halves of the two collapsing vortices rather than the reconnected original vortex lines formed after crossing in [59]. In our case, the longitudinal currents assist mutual twisting of the resulting vortices. In contrast, in [59] the ends of vortices reconnected

after the first intersection, are forced by the transverse currents into the second crossing configuration and then recombine into departing original vortices. It is possible that interactions with surrounding vortices, implicitly accounted in our case, affect the vortex cutting process.

During the collision, the twisting of vortices relaxes and after the reconnection their mutual velocity increases due to the line tension, which stretches vortices towards the parallel configuration causing their repulsion. Hence, the retardation of vortex motion due to the intersection of normal cores, which is expected to produce a local minimum in the system’s energy, does not occur. Instead, there is an increase of the energy of vortices due to the strong bending resulting in their slowdown before crossing. The addition of pinning centers near the intersection point should considerably increase the potential of crossing due to vortex bending and further delay the reconnection event. This will result in substantially stronger retardation of the crossing flux entry as we observe in our experiment.

An interesting phenomenon observed in our simulations is the appearance and expansion of left-handed helices (Fig. 18). The left-handed helices are twisted against the chirality expected for the screening currents induced by the applied B_{\perp} and flowing antiparallel to the polarity of in-plane vortices. The nucleation and expansion of such helices agree with Clem’s prediction of the “left-handed” helical instability in longitudinal transport currents [61]. Clem perceived this instability as a triggering mechanism for both flux cutting and depinning [17]. Brandt [62] showed that a similar helical instability should occur in the vortex lattices under parallel current. Later, Genenko [63] analyzed the behavior of helical vortices accounting for the surface barrier. Clearly, our simulations for the diluted vortex configuration confirm the predictions of the “left-handed” helical instability.

The picture of the twist of vortices due to the entry of semiloops from the surface and appearance and expansion of

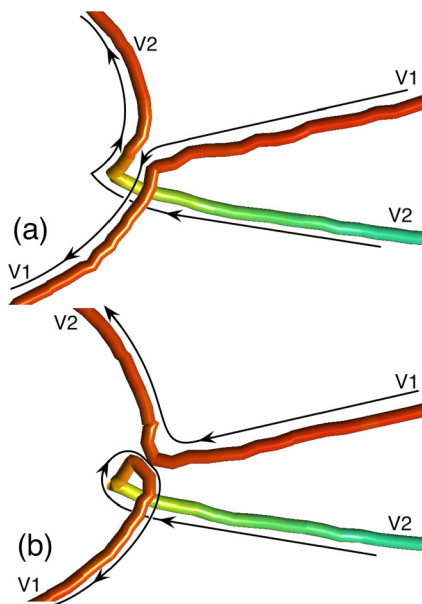


FIG. 17. (Color online) Vortex crossing and reconnection resolved with fine time steps ($0.1\tau_{GL}$). $B_x = 0.04$ and $B_z = 0.003$. Vortices twist near the crossing point (a), $t = 31\,999.2$ and reconnect after collapse of antiparallel segments forming tight loop on one of them (b), $t = 31\,999.3$. Strong bending of vortices prior to the collapse decelerate their mutual approach. However, in close vicinity, the local attraction of the antiparallel segments and their collapse, followed by untwisting of the strongly bent vortex lines, accelerate vortices. So, there is no delay expected for the moment of intersection of vortex cores.

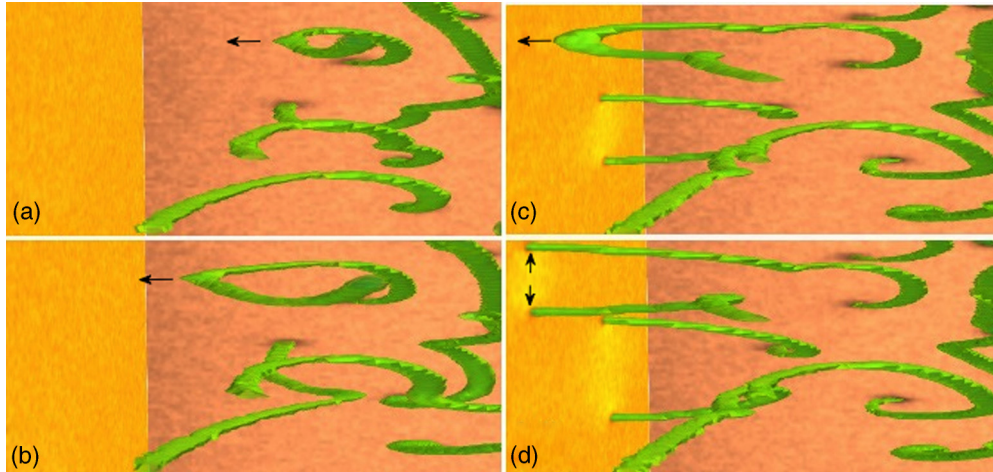


FIG. 18. (Color online) Expansion and exit to the surface of left-handed helical vortex (marked by arrow). $B_x = 0.04$, $B_z = 0.01$. (a) $t = 22750$, (b) $t = 23150$ (c) $t = 23850$, and (d) $t = 23900$. Multiple crossing and reconnection events occur during this time around the helix.

helical vortices, followed by their crossing and reconnection with initial vortex lines, corrects the scenario of oppositely moving vortex sublattices proposed in [12,44].

X. CONCLUSIONS

We performed MO imaging of flux distribution in a high-quality thin rectangular crystal of YBCO under crossing fields of different orientations. The observed flux patterns reveal strong penetration anisotropy of the normal flux B_{\perp} in the presence of the in-plane field \mathbf{H}_{\parallel} . A much faster propagation of B_{\perp} occurs along \mathbf{H}_{\parallel} , which can be associated with a specific structure of tilted vortices acquiring staircase shape of in-plane Josephson-like segments and carrying normal flux pancake vortices. Pancakes are strongly coupled to the Josephson-like strings and can easily move along them, transporting normal flux inside the sample. At the same time, the entry of tilted vortices from the sample edges aligned with \mathbf{H}_{\parallel} is strongly suppressed due to the motion of sharp flux fronts that carry enhanced longitudinal supercurrents. At these fronts, vortex motion is efficiently retarded due to the flux-cutting process, which essentially enhances the longitudinal current at the front.

Upon increasing the normal field, the length of the in-plane vortex segments decreases and vortices transform into curved pancake stacks. At this stage, the anisotropy of B_{\perp} motion disappears, and a traditional normal flux pattern, characteristic for isotropic critical currents in the ab plane, develops.

At crossing field magnetization of the sample with trapped vortices, we directly visualize the suppression of the initial flux due to entry of vortices of different orientation. This confirms Clem's conclusion that flux cutting results in flux consumption.

The TDGL simulations of the vortex behavior in the crossing fields reveal fine details of the flux-cutting process. It occurs when new vortex semiloops and expanding left-handed vortex helices intersect with initial vortices. Prior to intersection, misaligned vortices strongly bend locally around the crossing point, then merge, cut, and reconnect moving apart and forming tilted vortex lines. The main delay of the vortex motion occurs during their mutual bending. It increases the energy of vortices and forms potential maximum characterizing the cutting process. The later stage of the crossing and reconnection occurs with acceleration due to the local attraction of vortices and then due to their straightening forced by the line tension. We expect that the account for pinning that obstructs the vortex bending can essentially enhance the flux cutting potential and cause a stronger retardation of the crossing flux entry as we observe in our experiment.

ACKNOWLEDGMENTS

This work was supported by the U.S. Department of Energy, Office of Science, Materials Sciences and Engineering Division and Office of Advanced Scientific Computing Research, Scientific Discovery through Advanced Computing (SciDAC) program.

-
- [1] C. P. Bean, *Rev. Mod. Phys.* **36**, 31 (1964).
 - [2] C. P. Bean and J. D. Livingston, *Phys. Rev. Lett.* **12**, 14 (1964).
 - [3] L. Burlachkov, V. B. Geshkenbein, A. E. Koshelev, A. I. Larkin, and V. M. Vinokur, *Phys. Rev. B* **50**, 16770 (1994).
 - [4] E. Zeldov, A. I. Larkin, V. B. Geshkenbein, M. Konczykowski, D. Majer, B. Khaykovich, V. M. Vinokur, and H. Shtrikman, *Phys. Rev. Lett.* **73**, 1428 (1994).
 - [5] E. H. Brandt, *Phys. Rev. B* **60**, 11939 (1999).
 - [6] A. Gurevich, *Int. J. Mod. Phys. B* **09**, 1045 (1995).
 - [7] R. Boyer, G. Fillion, and M. A. R. LeBlanc, *J. Appl. Phys.* **51**, 1692 (1980).
 - [8] J. Clem, *Phys. Rev. B* **26**, 2463 (1982).
 - [9] J. R. Clem and A. Perez-Gonzales, *Phys. Rev. B* **30**, 5041 (1984).
 - [10] L. M. Fisher, S. E. Savel'ev, and V. A. Yampol'skii, *Physica C* **336**, 85 (2000).
 - [11] A. M. Campbell and J. E. Evetts, *Adv. Phys.* **21**, 199 (1972).
 - [12] J. Clem, *J. Low Temp. Phys.* **38**, 353 (1980).

- [13] A. Perez-Gonzales and J. Clem, *J. Appl. Phys.* **58**, 4326 (1985).
- [14] C. Romero-Salazar and F. Perez-Rodriguez, *Appl. Phys. Lett.* **83**, 5256 (2003); *Physica C* **404**, 317 (2004).
- [15] A. Badia and C. Lopez, *Phys. Rev. Lett.* **87**, 127004 (2001); *Phys. Rev. B* **65**, 104514 (2002).
- [16] A. M. Campbell, *Supercon. Sci. Technol.* **24**, 091001 (2011).
- [17] J. Clem, *Phys. Rev. B* **83**, 214511 (2011).
- [18] R. Cortes-Maldonado, O. De la Pena-Seaman, V. Garcia-Vazquez, and F. Perez-Rodriguez, *Supercon. Sci. Technol.* **26**, 125001 (2013).
- [19] M. V. Indenbom, A. Forkl, B. Ludescher, H. Kronmuller, H.-U. Habermeier, B. Leibold, G. D'Anna, T. W. Li, P. H. Kes, and A. A. Menovsky, *Physica C* **226**, 325 (1994).
- [20] M. V. Indenbom, C. J. van der Beek, V. Berseth, W. Benoi, G. D'Anna, A. Erb, E. Walker, and R. Flukiger, *Nature (London)* **385**, 702 (1997).
- [21] V. K. Vlasko-Vlasov, U. Welp, G. W. Crabtree, D. Gunter, V. V. Kabanov, V. I. Nikitenko, and L. M. Paulius, *Phys. Rev. B* **58**, 3446 (1998).
- [22] Ph. Vanderbemden, Z. Hong, T. A. Coombs, S. Denis, M. Ausloos, J. Schwartz, I. B. Rutel, N. H. Babu, D. A. Cardwell, and A. M. Campbell, *Phys. Rev. B* **75**, 174515 (2007).
- [23] V. K. Vlasko-Vlasov, U. Welp, G. W. Crabtree, and V. I. Nikitenko, in *Physics, and Materials Science of Vortex States, Flux Pinning, and Dynamics*, edited by R. Kossowsky, S. Bose, V. Pan, and Z. Durusoy (Kluwer, Dordrecht, 1999), Vol. 356, pp. 205–237.
- [24] V. K. Vlasko-Vlasov, U. Welp, G. W. Crabtree, D. Gunter, V. Kabanov, and V. I. Nikitenko, *Phys. Rev. B* **56**, 5622 (1997).
- [25] A. L. Rakhmanov, L. M. Fisher, V. A. Yampol'skii, M. Baziljevich, and T. H. Johansen, *Zh. Eksp. Teor. Fiz.* **122**, 886 (2002) [*Sov. Phys. JETP* **95**, 768 (2002)].
- [26] V. V. Moshchalkov and A. A. Zhukov, *Physica B* **169**, 601 (1991).
- [27] V. K. Vlasko-Vlasov, L. A. Dorosinskii, A. A. Polyanskii, V. I. Nikitenko, U. Welp, B. W. Veal, and G. W. Crabtree, *Phys. Rev. Lett.* **72**, 3246 (1994).
- [28] S. J. Park, J. S. Kouvel, H. B. Radousky, and J. Z. Liu, *Phys. Rev. B* **48**, 13998 (1993).
- [29] A. E. Koshelev, *Phys. Rev. B* **71**, 174507 (2005).
- [30] S. K. Hasanain, S. Manzoor, and A. Amirabadizadeh, *Supercon. Sci. Technol.* **8**, 519 (1995).
- [31] L. M. Fisher, A. V. Kalinov, S. E. Savel'ev, I. F. Voloshin, V. A. Yampol'skii, M. A. R. LeBlanc, and S. Hirscher, *Physica C* **278**, 169 (1997).
- [32] V. K. Vlasko-Vlasov, J. R. Clem, A. E. Koshelev, U. Welp, and W. K. Kwok, *Phys. Rev. Lett.* **112**, 157001 (2014).
- [33] E. H. Brandt, *Phys. Rev. Lett.* **68**, 3769 (1992).
- [34] B. I. Ivlev, Yu. N. Ovchinnikov, and V. L. Pokrovskii, *Mod. Phys. Lett. B* **05**, 73 (1991).
- [35] L. N. Bulaevskii, M. Ledvij, and V. G. Kogan, *Phys. Rev. B* **46**, 366 (1992).
- [36] M. Benkraouda and J. R. Clem, *Phys. Rev. B* **53**, 438 (1996).
- [37] A. E. Koshelev, *Phys. Rev. Lett.* **83**, 187 (1999).
- [38] E. H. Brandt and M. V. Indenbom, *Europhys. Lett.* **22**, 735 (1993).
- [39] E. Zeldov, J. R. Clem, M. McElfresh, and M. Darwin, *Phys. Rev. B* **49**, 9802 (1994).
- [40] G. P. Mikitik and E. H. Brandt, *Phys. Rev. B* **62**, 6800 (2000).
- [41] E. H. Brandt, *Rep. Prog. Phys.* **58**, 1465 (1995).
- [42] J. Clem, M. Weigand, J. H. Durrell, and A. M. Campbell, *Supercon. Sci. Technol.* **24**, 062002 (2011).
- [43] S. E. Savel'ev, L. M. Fisher, and V. A. Yampol'skii, *Zh. Eksp. Teor. Fiz.* **112**, 936 (1997) [*Sov. Phys. JETP* **85**, 507 (1997)].
- [44] L. M. Fisher, K. V. Il'enko, A. V. Kalinov, M. A. R. LeBlanc, F. Pérez-Rodríguez, S. E. Savel'ev, I. F. Voloshin, and V. A. Yampol'skii, *Phys. Rev. B* **61**, 15382 (2000).
- [45] A. Badía-Majós, C. López, and H. S. Ruiz, *Phys. Rev. B* **80**, 144509 (2009).
- [46] E. H. Brandt and G. P. Mikitik, *Physica C* **404**, 69 (2004).
- [47] E. H. Brandt and G. P. Mikitik, *Supercon. Sci. Technol.* **17**, S1 (2004).
- [48] G. P. Mikitik and E. H. Brandt, *Phys. Rev. B* **69**, 134521 (2004).
- [49] G. P. Mikitik and E. H. Brandt, *Phys. Rev. B* **71**, 012510 (2005).
- [50] E. H. Brandt and G. P. Mikitik, *Supercon. Sci. Technol.* **20**, S111 (2007).
- [51] E. H. Brandt and G. P. Mikitik, *J. Phys. Conf. Ser.* **150**, 052024 (2009).
- [52] D. G. Walmsley, *J. Phys. F* **2**, 510 (1972).
- [53] E. H. Brandt, J. R. Clem, and D. G. Walmsley, *J. Low Temp. Phys.* **37**, 43 (1979).
- [54] P. Wagenleithner, *J. Low Temp. Phys.* **48**, 25 (1982).
- [55] A. Sudbo and E. H. Brandt, *Phys. Rev. Lett.* **67**, 3176 (1991).
- [56] M. A. Moore and N. K. Wilkin, *Phys. Rev. B* **50**, 10294 (1994).
- [57] M. J. W. Dodgson and M. A. Moore, *Phys. Rev. B* **51**, 11887 (1995).
- [58] C. Carraro and D. S. Fisher, *Phys. Rev. B* **51**, 534 (1995).
- [59] M. Bou-Diab, M. J. W. Dodgson, and G. Blatter, *Phys. Rev. Lett.* **86**, 5132 (2001).
- [60] I. A. Sadovskyy, A. E. Koshelev, C. L. Phillips, D. A. Karpeev, and A. Glatz, *arXiv:1409.8340*.
- [61] J. Clem, *Phys. Rev. Lett.* **38**, 1425 (1977).
- [62] E. H. Brandt, *J. Low Temp. Phys.* **44**, 33 (1981); **44**, 59 (1981).
- [63] Y. A. Genenko, *Phys. Rev. B* **51**, 3686 (1995); **53**, 11757 (1996).